

## Comparison of photocatalytic activity for different co-precipitated spinel ferrites

Andris Sutka · Martins Millers · Martins Vanags ·  
Urmas Joost · Mihael Maiorov · Vambola Kisand ·  
Rainer Pärna · Inna Juhnevica

Received: 11 June 2014 / Accepted: 21 October 2014 / Published online: 4 March 2015  
© Springer Science+Business Media Dordrecht 2015

**Abstract** The present work reports the co-precipitation synthesis and photocatalytic activity of  $MFe_2O_4$  ( $M = Ni, Zn, Co, Cu, Mg$ ) nanopowders. To compare their properties, all the powders were synthesized under similar synthesis conditions. Their structures and properties were determined by X-ray diffraction, scanning electron microscopy, X-ray photoelectron spectroscopy, UV–Vis diffuse reflectance spectra, nitrogen adsorption–desorption, and vibrating sample magnetometry. The results revealed the formation of single-phase spinel-structure magnetic nanoparticles with particle size  $<10$  nm. All the samples exhibited strong light absorption in the visible range. Among the investigated nanopowders, nickel ferrite showed the highest photocatalytic activity and dye adsorption. The change in the light absorption intensity after 3 h of visible light irradiation of the dye over the  $NiFe_2O_4$  photocatalyst reached  $\sim 70$  %.

**Keywords** Spinel ferrite · Photocatalytic · Co-precipitation

---

A. Sutka (✉) · M. Millers · I. Juhnevica  
Faculty of Materials Sciences and Applied Chemistry, Riga Technical University, Paula Valdena  
3/7, Riga LV-1048, Latvia  
e-mail: andris.sutka@rtu.lv

M. Vanags  
Institute of Solid State Physics, University of Latvia, Kengaraga 8, Riga LV-1063, Latvia

U. Joost · V. Kisand · R. Pärna  
Institute of Physics, University of Tartu, Ravila 14c, 50411 Tartu, Estonia

U. Joost · V. Kisand · R. Pärna  
Estonian Nanotechnology Competence Center, Ravila 14c, 50411 Tartu, Estonia

M. Maiorov  
Institute of Physics, University of Latvia, Miera 32, Salaspils 2169, Latvia

## Introduction

Research on new photocatalysts for pollutant degradation or water splitting to store solar energy is of great interest in both science and technology. Photocatalysts should be visible-light active, magnetically separable, and stable against photocorrosion [1]. Spinel ferrites are promising materials for these purposes due to their low bandgap energy [2], ferrimagnetic [3] or superparamagnetic [4] behaviour, and structural stability [5]. The physical and chemical properties of the ferrites are strongly influenced by their chemical composition [6], cation distribution between sub-lattice sites [7], and synthesis method [8], as well as the type and concentration of the point defects in the spinel structure, which can be regulated by controlling the stoichiometry or preparation conditions [9–12].

The spinel ferrite structure can be described as a cubic close-packed arrangement of oxygen atoms in which 32 oxygen ions form a unit cell. Layers of oxygen ions contain 64 tetrahedral sites and 32 octahedral sites. To provide electrical neutrality of the lattice, the 8 tetrahedral and 16 octahedral sites are occupied by divalent or trivalent ions, so a unit cell contains 8  $MFe_2O_4$  formula units [13]. It is possible to regulate spinel ferrite properties to a large extent by changing the chemical composition, because M in the formula  $MFe_2O_4$  can be an Fe, Ni, Zn, Co, Cu, Li, Mg, Cd, Mn, Cr, or Ca ion, or these ions can even be combined as in  $Ni-ZnFe_2O_4$ , for example. The properties of spinel ferrites can also be regulated by changing the distribution of the divalent and trivalent cations between the tetrahedral and octahedral sites [7]. Spinel ferrites can be expressed by the formula  $(M_\delta Fe_{1-\delta})(M_{1-\delta} Fe_{1+\delta})O_4$ , where  $\delta$  is the inversion degree. The normal spinel structure with  $\delta = 1$  has tetrahedral sites occupied by divalent cations, while octahedral sites are occupied by trivalent cations. In the inverse spinel structure with  $\delta = 0$ , the divalent cations occupy octahedral sites, while the trivalent cations are distributed among the tetrahedral and octahedral sites. In a mixed spinel structure with  $\delta$  between 1 and 0, both the tetrahedral and the octahedral sub-lattice sites are occupied by divalent and trivalent ions [13]. A typical spinel ferrite with a normal spinel structure is  $ZnFe_2O_4$ .

Many different spinel ferrite compounds have recently demonstrated reasonable visible-light photocatalytic activity [14]. Zn-, Ni-, Mg-, Cu-, and Co-spinel ferrites have attracted the greatest interest because they exhibit not only decent visible-light activity but also ferrimagnetic or superparamagnetic properties. However, spinel ferrites have shown diverse photocatalytic efficiency in different investigations. Cheng et al. [15] demonstrated that zinc ferrite can be almost inactive, while Guo et al. [16] showed high visible-light activity by complete degradation of methylene blue (MB) in 150 min. As the physical and chemical properties of spinel ferrites are strongly affected by the synthesis conditions and method, because these influence the chemical composition, stoichiometry, point defect concentration, and cation distribution, we decided to synthesize different spinel compounds under similar synthesis conditions to compare their photocatalytic properties.

## Experimental

Spinel ferrites of  $MFe_2O_4$  (where M = Zn, Ni, Mg, Cu, or Co) were synthesized by the co-precipitation method. Reagent grade  $Zn(NO_3)_2 \cdot 6H_2O$ ,  $Ni(NO_3)_2 \cdot 6H_2O$ ,

$\text{Mg}(\text{NO}_3)_2 \cdot 6\text{H}_2\text{O}$ ,  $\text{Cu}(\text{NO}_3)_2 \cdot 3\text{H}_2\text{O}$ ,  $\text{Co}(\text{NO}_3)_2 \cdot 6\text{H}_2\text{O}$ ,  $\text{Fe}(\text{NO}_3)_3 \cdot 9\text{H}_2\text{O}$ , and NaOH were used as received from Sigma Aldrich. Each metal nitrate was dissolved separately in distilled water. The solution molarity was 0.2 and 0.4 M for  $\text{M}(\text{NO}_3)_2 \cdot x\text{H}_2\text{O}$  and  $\text{Fe}(\text{NO}_3)_3 \cdot 9\text{H}_2\text{O}$ , respectively. The solutions were mixed together. A 5-M NaOH solution in water was used as a precipitator and added dropwise to increase the pH above 12. Then, the mixture was heated up to 80 °C and stirred for 3 h. The precipitates obtained after stirring were filtered, washed with distilled water, and dried at 60 °C for 24 h. After drying, parts of the powders were annealed at 150, 300, 450, and 600 °C for 3 h.

The crystal structure of the obtained nanopowders was characterized with an Ultima+X-ray diffractometer (Rigaku, Japan) with  $\text{CuK}\alpha$  radiation. Microstructural features were analysed by high resolution scanning electron microscopy (SEM) (Helios Nanolab, FEI) and nitrogen adsorption–desorption (NOVA 1200e; Quantachrome, UK). Magnetic properties were measured by a vibrating sample magnetometer (VSM) (Model 7404 VSM; Lake Shore Cryotronic, USA).

To measure the light absorbance of nanopowder samples, a UV–Visible Shimadzu UV-3700 spectrophotometer (Shimadzu Scientific Instruments, Kyoto, Japan) with a barium sulfate-coated integrating sphere ISR-240A (wavelength range from 240 to 800 nm) was used. With integrating spheres, the measurement is performed by placing the sample in front of the incident light, which reflects from the sample in all directions (diffuse scattering) inside a sphere coated with barium sulfate, and is collected with the detector at the end. The obtained relative reflectance  $R_\infty$  with respect to the reflectance of the reference standard (barium sulfate) was taken to be 100 %. A Kubelka–Munk function conversion is applied to the diffuse reflectance spectrum to compensate for differences in the raw diffuse reflectance spectrum from its transmission equivalent [17].

The Fourier transmission infrared (FTIR) absorption spectra of dried nickel ferrite sample were recorded in the range from 400 up to 4000  $\text{cm}^{-1}$  using a Shimadzu Prestige 21 spectroscope (Japan). Sample preparation included mixing ferrite powder with dried KBr powder and pellet formation.

X-ray photoelectron spectroscopy (XPS) was used to investigate the chemical state and elemental composition of sample nanopowders. XPS measurements were conducted using a surface station equipped with an electron energy analyser (SCIENTA SES 100) and a non-monochromatic twin anode X-ray tube (Thermo XR3E2), with characteristic energies of 1253.6 eV (Mg  $\text{K}_{\alpha 1,2}$  FWHM 0.68 eV) and 1486.6 eV (Al  $\text{K}_{\alpha 1,2}$  FWHM 0.83 eV). All XPS measurements were conducted in ultra-high vacuum (UHV) conditions. Raw data were processed using Casa XPS software. Data processing involved the removal of  $\text{K}_\alpha$  and  $\text{K}_\beta$  satellites, removal of background, and fitting of components. Background removal was done using a Shirley background, and a Gauss–Lorentz hybrid function was used for fitting (GL 70, Gauss 30 %, Lorentz 70 %) to obtain the best fit. However, the absolute amounts of different compounds have to be considered cautiously and are given as estimates only.

The photocatalytic activities were evaluated by degradation of MO dye in an aqueous solution under visible light. A light-emitting diode (LED) 100-W light source Visional IP65 (see Fig. 1 for the measured emission spectrum of the light

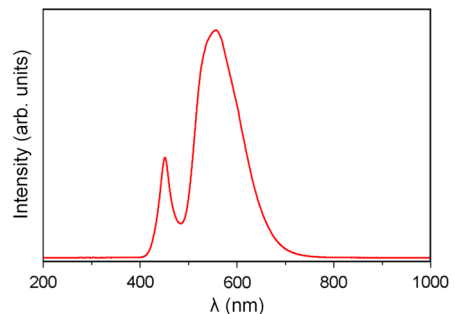
source) was used. The initial concentration of MO in a closed polystyrene reaction vessel was fixed at 10 mg/l with a photocatalyst loading of 1 g/l. The rate of MO dye degradation was monitored after certain time intervals by taking 1 ml of sample from each set, centrifuging, and analysing it using the spectrophotometer. Dye degradation was controlled by the MO concentration change  $C/C_0$  by measuring the absorbance at maximum wavelength ( $\lambda_{\max}$ ) of MO dye.  $C$  and  $C_0$  are absorbance values at maximum wavelength after and before photocatalytic activity measurement, respectively.

## Results and discussion

The SEM micrographs of the co-precipitation-derived nanopowders (without annealing) are shown in Fig. 2. SEM micrographs demonstrate that the nanopowders mostly consist of agglomerated nanoparticles with a size of <10 nm. From the SEM micrograph of the co-precipitated  $\text{MgFe}_2\text{O}_4$  sample, it was not possible to distinguish individual nanoparticles, which was attributed to the small size of the particles or the amorphous nature of the synthesized powder, as demonstrated by XRD. After annealing, the particle size increased in all samples. As an example, the SEM micrograph shown for the  $\text{NiFe}_2\text{O}_4$  sample (Fig. 1) annealed at 600 °C for 3 h confirms particle growth during annealing.

Figure 3 shows the XRD diffractograms of the different co-precipitated ferrite nanopowders. Co-precipitated  $\text{CoFe}_2\text{O}_4$ ,  $\text{CuFe}_2\text{O}_4$ , and  $\text{ZnFe}_2\text{O}_4$  samples exhibit XRD peaks at  $2\theta \sim 18^\circ$ ,  $\sim 30^\circ$ ,  $\sim 35.5^\circ$ ,  $\sim 37^\circ$ ,  $\sim 43^\circ$ ,  $\sim 54^\circ$ , and  $\sim 57^\circ$ , which can be indexed to reflection from the (111), (220), (311), (222), (400), (422), and (511) planes of the cubic spinel crystal structure, respectively. Additional XRD peaks from impurity phases were not observed in any of the samples. XRD patterns of the  $\text{NiFe}_2\text{O}_4$  and  $\text{MgFe}_2\text{O}_4$  samples do not show sharp reflexions, which could be attributed to the small size of the synthesized particles or the amorphous nature of the synthesized products. However, crystallinity cannot be estimated correctly from measured XRD patterns due to peak broadening arising from small particle size. The mean crystallite sizes ( $D$ ) of the samples, listed in Table 1, were calculated by using the well-known Scherrer's formula from the full-width at half-maximum of the (311) plane. As can be seen from Table 1, the highest average size of crystallites

**Fig. 1** Measured spectra of light source used for photocatalytic experiments



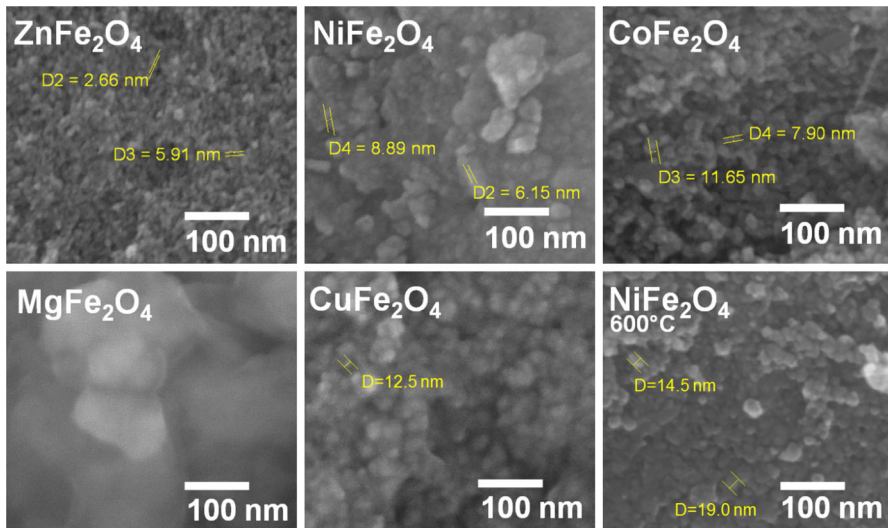


**Fig. 2** SEM micrographs of different co-precipitated ferrite samples (without annealing). The image in the *bottom right corner* shows the SEM micrograph of NiFe<sub>2</sub>O<sub>4</sub> co-precipitated powder annealed at 600 °C for 3 h

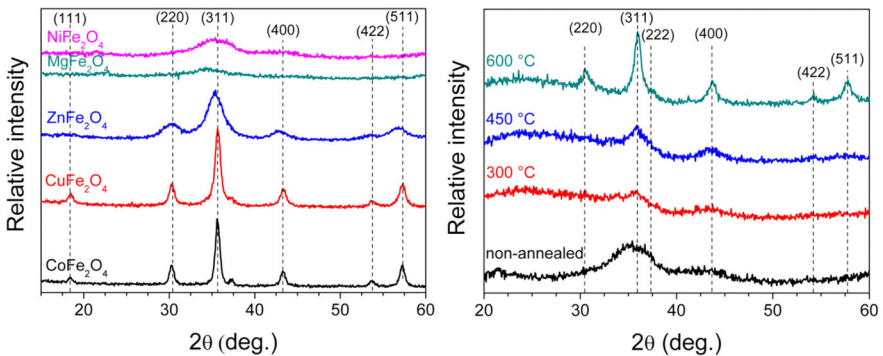


**Fig. 3** XRD patterns of co-precipitated spinel ferrite samples without annealing (*left*) and XRD pattern of co-precipitated NiFe<sub>2</sub>O<sub>4</sub> sample annealed at different temperatures for 3 h (*right*)

can be observed for CoFe<sub>2</sub>O<sub>4</sub> and CuFe<sub>2</sub>O<sub>4</sub> and the smallest for MgFe<sub>2</sub>O<sub>4</sub> and NiFe<sub>2</sub>O<sub>4</sub> samples.

The XRD patterns of NiFe<sub>2</sub>O<sub>4</sub> photocatalysts annealed at different temperatures are shown in Fig. 3. By increasing the annealing temperature for the co-precipitated NiFe<sub>2</sub>O<sub>4</sub> nanopowders, the intensity of the XRD peak indexed to reflection from (311) plane increases, thus confirming increased crystallinity. The formation of complete spinel NiFe<sub>2</sub>O<sub>4</sub> structure was observed after annealing at 600 °C. Samples annealed at 600 °C exhibited XRD peaks which were indexed to reflections from the (220), (311), (222), (400), (422), and (511) planes of the cubic spinel crystal structure.

**Table 1** Properties of co-precipitated spinel ferrite photocatalysts

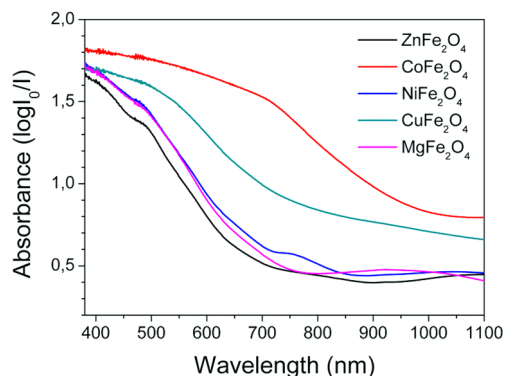
Ferrite	$D$ (nm)	$a$ (Å)	$\sigma_{\text{BET}}$ (m <sup>2</sup> /g)	$E_g$ (eV)	$M_s$ (emu/g)	$H_c$ (Oe)
CoFe <sub>2</sub> O <sub>4</sub>	12.5	8.37	91	1.40	52.6	320.01
CuFe <sub>2</sub> O <sub>4</sub>	11.5	8.36	117	1.56	24.3	–
ZnFe <sub>2</sub> O <sub>4</sub>	4.5	8.44	134	2.06	3.8	10.03
MgFe <sub>2</sub> O <sub>4</sub>	2.3	–	135	1.91	1.8	20.01
NiFe <sub>2</sub> O <sub>4</sub>	2.0	8.41	83	1.91	2.5	20.03

The measured BET specific surface areas ( $\sigma_{\text{BET}}$ ) for different samples are depicted in Table 1. Powder samples exhibit a high specific surface area from 80 to 135 m<sup>2</sup>/g. The highest surface area of 134.9 m<sup>2</sup>/g was observed for MgFe<sub>2</sub>O<sub>4</sub>. The NiFe<sub>2</sub>O<sub>4</sub> sample with the smallest calculated crystallite sizes exhibited the smallest specific surface area. This discrepancy can be attributed to clustering and more closed packed agglomerate formation dominated by the effects of the drying colloidal solution of the small particles [18].

Figure 4 gives the UV–Vis absorption spectra (Kubelka–Munk function) of the different co-precipitated spinel ferrites. All samples exhibit strong light absorption in the visible range. The band gap energy necessary for the photoexcited electron transition from O 2*p* origin valence band top into the Fe 3*d* origin conduction band bottom in the spinel ferrite was found from the  $(\alpha h\nu)^2$  versus photon energy plot and is shown for different samples in Table 1. Band gap is found when a line drawn from the absorption edge of molecule crosses the *x*-axes. All samples exhibit bandgap energy lower than 2.1 eV, and therefore co-precipitated samples have suitable bandgap energy for solar light absorption.

Adsorption and degradation under visible light of MO dye in aqueous solution by different ferrite photocatalysts are shown in Fig. 5. As can be seen, the photocatalytic activity of various spinel ferrite samples decreases in the order CuFe<sub>2</sub>O<sub>4</sub> < CoFe<sub>2</sub>O<sub>4</sub> < ZnFe<sub>2</sub>O<sub>4</sub> < MgFe<sub>2</sub>O<sub>4</sub> < NiFe<sub>2</sub>O<sub>4</sub>. Nickel ferrite shows the highest photocatalytic activity between synthesized spinel ferrites. The degradation percentage after 3 h over the NiFe<sub>2</sub>O<sub>4</sub> photocatalyst reached ~70 %, while absorption changes of the MO solution in the presence of NiFe<sub>2</sub>O<sub>4</sub> in the dark after

**Fig. 4** UV–Vis absorption spectra (Kubelka–Munk function) for different co-precipitated spinel-type ferrite samples



3 h showed a decrease of absorption intensity by 26 %. Highest photocatalytic activity of  $\text{NiFe}_2\text{O}_4$  can be attributed to its higher MO dye adsorption. Nickel ferrite shows the highest dye adsorption among the samples, which can be attributed to its smaller crystallite and grain size observed by XRD and SEM analysis or its surface properties. Higher dye adsorption can be attributed to larger amounts of unsaturated bonds and defects on the  $\text{NiFe}_2\text{O}_4$  nanoparticle surface [19]. By decreasing the nanoparticle size, the amount of unsaturated bonds and surface defects increases, thus enhancing dye adsorption.

To obtain detailed information for the surface structure of the  $\text{NiFe}_2\text{O}_4$  sample, FTIR studies were performed. An infrared spectrum of the non-annealed  $\text{NiFe}_2\text{O}_4$  sample was recorded in the range  $4000\text{--}400\text{ cm}^{-1}$  (Fig. 6). In the region  $4000\text{--}3000\text{ cm}^{-1}$ , a strong and broad absorption band was observed with a maximum at  $3380\text{ cm}^{-1}$ . This band can be associated with the non-bonded hydroxyl species [20]. The FTIR spectrum is also showing the presence of  $\text{--OH}$  groups (absorption at around  $1000\text{ cm}^{-1}$ ). The FTIR spectrum also shows peaks at  $1625$ ,  $1488$  and  $1355\text{ cm}^{-1}$ , which can be assigned to a carboxylate ( $\text{COO}^-$ ) stretch [21–23]. Most of the carbon is adventitious carbon adsorbed on the sample from the atmosphere. The absorption band at  $\sim 2340\text{ cm}^{-1}$  corresponds to KBr.

Intrinsic stretching vibrations of metal cations in crystallographic sites of spinel structure were also observed for the non-annealed  $\text{NiFe}_2\text{O}_4$  sample, which confirms

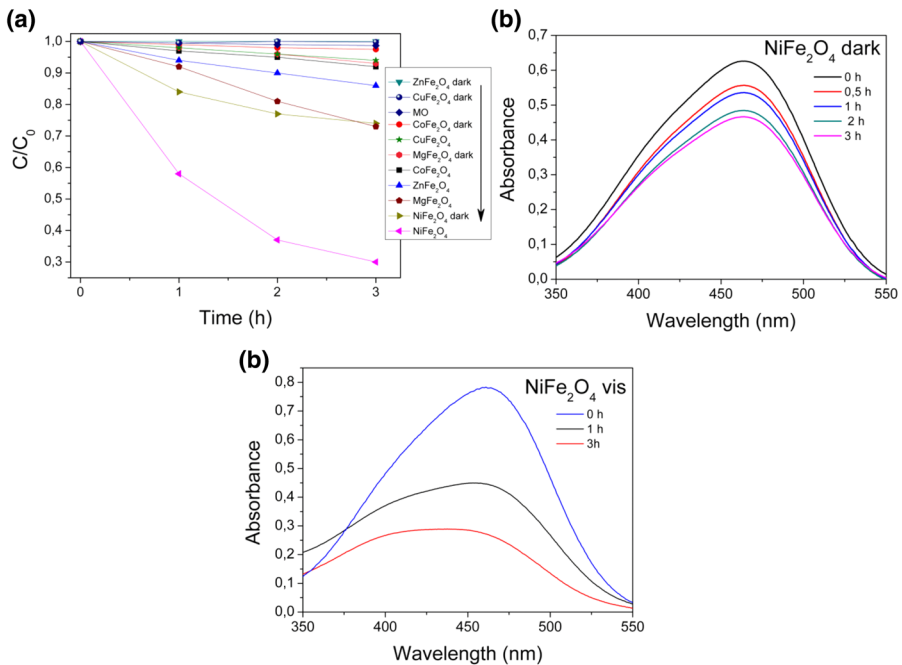
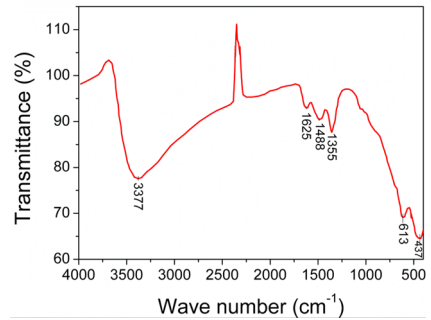


**Fig. 5** Adsorption and photodegradation during visible light irradiation of MO over time by using various synthesized spinel ferrite photocatalysts (a), absorbance changes of MO solution in the presence of  $\text{NiFe}_2\text{O}_4$  in the dark (b), and under visible light irradiation (c)

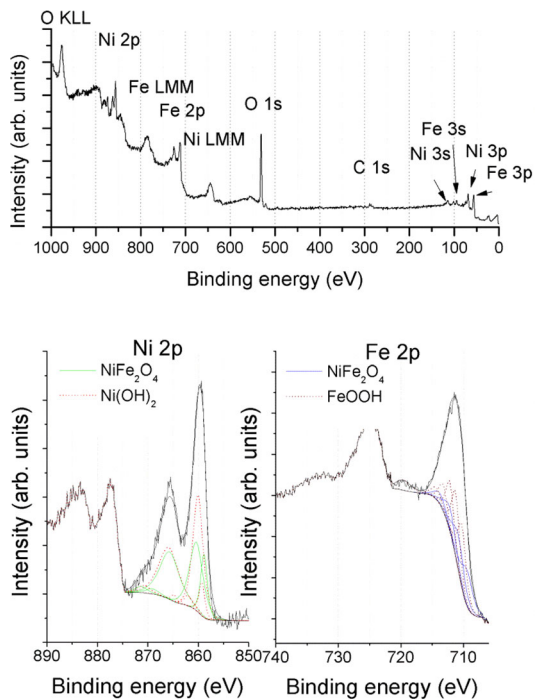
**Fig. 6** IR spectrum of the non-annealed  $\text{NiFe}_2\text{O}_4$  sample



the spinel structure formation. Two main metal–oxygen bands in the spinel ferrites are located below  $1000 \text{ cm}^{-1}$  [24]. In our synthesized  $\text{NiFe}_2\text{O}_4$  sample, the highest one ( $V_1$ ) is observed at  $613 \text{ cm}^{-1}$  and the lower one ( $V_2$ ) at  $437 \text{ cm}^{-1}$ .  $V_1$  is assigned to intrinsic stretching vibrations of the metal cation at the tetrahedral site  $M_{\text{tetra}} \leftrightarrow \text{O}$ , while  $V_2$  corresponds to the metal cation at the octahedral site  $M_{\text{octa}} \leftrightarrow \text{O}$  [25].

The non-annealed  $\text{NiFe}_2\text{O}_4$  sample was analysed more closely by XPS. The Ni  $2p$  and Fe  $2p$  XPS spectra (Fig. 7) of  $\text{NiFe}_2\text{O}_4$  demonstrated several deviations from the spectra of pristine  $\text{NiFe}_2\text{O}_4$ . The Fe  $2p$  XPS spectrum of  $\text{NiFe}_2\text{O}_4$  was well fitted (according to the residual STD value) by using a multiplet structure of  $\text{FeO}(\text{OH})$  ( $\text{Fe}^{3+}$ ); however, the presence of a small amount of iron oxide on the sample surface

**Fig. 7** XPS overview spectrum of  $\text{NiFe}_2\text{O}_4$  co-precipitated nanopowder (upper panel) and detailed photoelectron spectra of Ni  $2p$  (bottom left) and Fe  $2p$  (bottom right)





cannot be excluded. Ni 2*p* XPS spectra of NiFe<sub>2</sub>O<sub>4</sub> heterostructure were a combination of NiFe<sub>2</sub>O<sub>4</sub> and Ni(OH)<sub>2</sub> [26], which are compounds that contain Ni<sup>2+</sup>, but Ni<sup>3+</sup> was not observed in the XPS spectra. Overall, the NiFe<sub>2</sub>O<sub>4</sub> particles are covered with Ni(OH)<sub>2</sub> and FeO(OH), as can be concluded from the analysis of Ni 2*p* and Fe 2*p* photo lines. The formation of hydroxides on the NiFe<sub>2</sub>O<sub>4</sub> particles might be due to the synthesis conditions of the particles (aqueous solutions) and/or storage in the ambient atmosphere. The large amount of hydroxyl groups on the surface of the NiFe<sub>2</sub>O<sub>4</sub> particles would produce reactive radicals, such as ·OH, and H<sub>2</sub>O<sub>2</sub>, further increasing the activity of the material. Such active radicals can react with organic compounds and oxidize or reduce them [27].

The influence of the annealing temperature was studied for the three most active synthesised photocatalysts (Fig. 8)—NiFe<sub>2</sub>O<sub>4</sub>, MgFe<sub>2</sub>O<sub>4</sub> and ZnFe<sub>2</sub>O<sub>4</sub>. The results indicated that the photocatalytic activity of the tested samples decreases when additional annealing is performed, which could be attributed to particle growth and the decrease of the specific surface area. However, after heating at 600 °C, the photocatalytic activity increases again to a small extent in all samples. The increase in the photocatalytic activity after annealing at 600 °C can be attributed to the increase of the crystallinity and the decrease of the defect concentration in the material. It has been reported that almost all typical crystal defects such as grain boundaries, dislocations, native point defects, and substitutional impurities are expected to promote the scattering and recombination of carriers. Improved crystallinity leads to reduced recombination and bulk transport of charge carriers attributed to fewer non-equilibrium defects in the photocatalyst [28]. Improved crystallinity for NiFe<sub>2</sub>O<sub>4</sub> sample during annealing is confirmed by XRD studies (Fig. 3 (right)).

All synthesized ferrite samples (without annealing) exhibited ferrimagnetic or superparamagnetic behaviour (Fig. 9). However, NiFe<sub>2</sub>O<sub>4</sub>, MgFe<sub>2</sub>O<sub>4</sub>, and ZnFe<sub>2</sub>O<sub>4</sub> particles exhibited weak magnetization, and thus only CoFe<sub>2</sub>O<sub>4</sub> or CuFe<sub>2</sub>O<sub>4</sub> particles could be collected by the external magnetic field. The saturation magnetization (*M<sub>s</sub>*) and coercive force (*H<sub>c</sub>*) values of different samples are given in Table 1. The small *M<sub>s</sub>* values of NiFe<sub>2</sub>O<sub>4</sub> and MgFe<sub>2</sub>O<sub>4</sub> samples could be attributed to small particle size, but in the case of ZnFe<sub>2</sub>O<sub>4</sub> sample, the low *M<sub>s</sub>* value was due to its antiferromagnetic behaviour [7].

**Fig. 8** Influence of the annealing temperature on photocatalytic activity of different synthesized photocatalysts

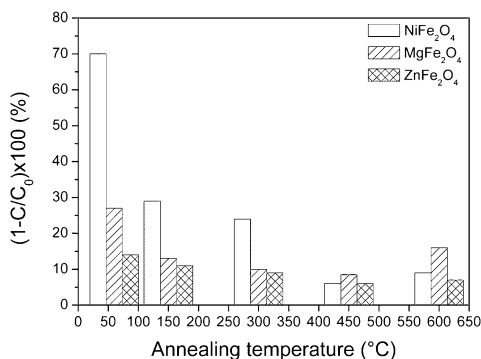
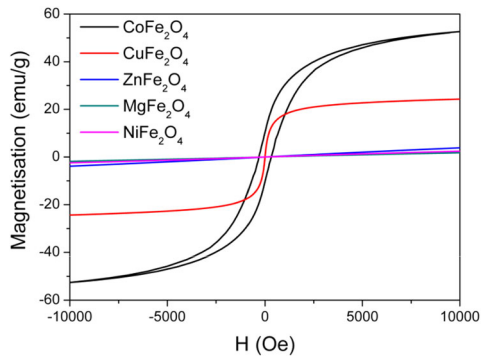


**Fig. 9** Room temperature M–H curves of non-annealed co-precipitated spinel ferrite nanopowders



## Conclusions

This investigation provided a facile approach to the synthesis of visible-light active magnetic spinel ferrite nanoparticles. The single-phased spinel structure was formed after the co-precipitation reaction and drying at 60 °C (without further annealing). The photocatalytic degradation of MO under visible light indicates that NiFe<sub>2</sub>O<sub>4</sub> is the most efficient among the synthesized photocatalysts. The light absorption intensity change after 3 h of visible-light irradiation of the dye over the NiFe<sub>2</sub>O<sub>4</sub> photocatalyst reached ~70 %. FTIR and XPS analysis revealed the formation of hydroxides on the NiFe<sub>2</sub>O<sub>4</sub> particles, which would enhance the formation of reactive radicals such as ·OH and H<sub>2</sub>O<sub>2</sub>. Overall, since co-precipitated ferrite nanopowders exhibit visible light photocatalytic activity and magnetic properties, it can be considered that they may have potential applications in the field of photodegradation of organic pollutants.

**Acknowledgments** The authors gratefully acknowledge the financial support by the European Social Fund within the project ‘Elaboration of Innovative Functional Materials and Nanomaterials for Application in Environment Control Technologies’ IDP/1.1.1.2.0/13/APIA/VIAA/30. Financial support by the Estonian Ministry of Education and Research (target-financed theme IUT2-25) and the Estonian Nanotechnology Competence Centre (EU29996) is also gratefully acknowledged.

## References

1. G. Liu, F. He, J. Zhang, L. Li, F. Li, L. Chen, Y. Huang, *Appl. Catal. B Environ.* **150–151**, 515 (2014)
2. S.M. Chavan, M.K. Babrekar, S.S. More, K.M. Jadhav, *J. Alloys Compd.* **507**, 21 (2010)
3. J.D. Adam, L.E. Davis, G.F. Dionne, E.F. Schloemann, S.N. Stitzer, *IEEE Trans. Microw. Theory* **50**, 721 (2002)
4. A.J. Rondinone, A.C.S. Samia, Z.J. Zhang, *J. Phys. Chem. B* **103**, 6876 (1999)
5. P. Guo, G. Zhang, J. Yu, H. Li, X.S. Zhao, *Colloids Surf. A* **395**, 168 (2012)
6. I.H. Gul, W. Ahmed, A. Maqsood, *J. Magn. Magn. Mater.* **320**, 270 (2008)
7. A. Šutka, R. Pärna, M. Zamovskis, V. Kisand, G. Mezinskis, J. Kleperis, M. Maiorov, D. Jakovlev, *Phys. Status Solidi A* **210**, 1892 (2013)
8. S. Gyergyek, D. Makovec, A. Kodre, I. Arčon, M. Jagodič, M. Drogenik, *J. Nanopart. Res.* **12**, 1263 (2010)
9. A. Sutka, G. Mezinskis, A. Lulis, D. Jakovlevs, *Sens. Actuator B Chem.* **171–172**, 204 (2012)

10. A. Sutka, *Sens. Lett.* **11**, 2010 (2013)
11. T.P. Sumangala, C. Mahender, B.N. Sahu, N. Venkataramani, S. Prasa, *Phys. B* (2014). doi:[10.1016/j.physb.2014.03.086](https://doi.org/10.1016/j.physb.2014.03.086)
12. A. Šutka, R. Pärna, J. Kleperis, T. Käämbre, I. Pavlovska, V. Korsaks, K. Malnieks, L. Grinberga, V. Kisand, *Phys. Scr.* **89**, 044011 (2014)
13. R. Valenzuela, *Magnetic Ceramics*, 1st edn. (Cambridge, Melbourne, 1994)
14. E. Casbeer, V.K. Sharma, X.Z. Li, *Sep. Purif. Technol.* **87**, 1 (2012)
15. P. Cheng, W. Li, T. Zhou, Y. Jin, M. Gu, J. Photochem. Photobiol. C **168**, 97 (2004)
16. P. Guo, G. Zhang, J. Yu, H. Li, X.S. Zhao, *Colloids Surf. A* **395**, 168 (2012)
17. M. Khoshhesab, in: *Reflectance IR Spectroscopy, Infrared Spectroscopy—Materials Science, Engineering and Technology*, ed. by T. Theophanides, InTech (2012), pp. 1–13
18. Y.V. Kolen'ko, M. Bañobre-López, C. Rodríguez-Abreu, E. Carbó-Argibay, A. Sailsman, Y. Piñeiro-Redondo, M.F. Cerqueira, D.Y. Petrovykh, K. Kovnir, O.I. Lebedev, J. Rivas, *J. Phys. Chem. C* **118**, 8691 (2014)
19. R. Liu, X. Shen, X. Yang, Q. Wang, F. Yang, *J. Nanopart. Res.* **15**, 1679 (2013)
20. S.K. Shukla, G.K. Parashar, A.P. Mishra, P. Misra, B.C. Yadav, R.K. Shukla, L.M. Bali, G.C. Dubey, *Sens. Actuator B Chem.* **98**, 5 (2004)
21. A.L. Willis, N.J. Turro, S. O'Brien, *Chem. Mater.* **17**, 5970 (2005)
22. E. Manova, B. Kunev, D. Paneva, I. Mitov, L. Petrov, *Chem. Mater.* **16**, 5689 (2004)
23. M. Stefanescu, M. Stoia, T. Dippong, O. Stefanescu, P. Barvinschi, *Acta Chim. Slov.* **56**, 379 (2009)
24. A.M. El-Sayed, *Ceram. Int.* **28**, 363 (2002)
25. M.M. Mallapur, P.A. Shaikh, R.C. Kambale, H.V. Jamadar, P.U. Mahamuni, B.K. Chougule, *J. Alloys Compd.* **479**, 797 (2009)
26. M.C. Biesinger, B.P. Payne, A.P. Grosvenor, L.W.M. Lau, A.R. Gerson, R.S.C. Smart, *Appl. Surf. Sci.* **257**, 2717 (2011)
27. C. He, Y. Yu, X. Hu, A. Larbot, *Appl. Surf. Sci.* **200**, 239 (2002)
28. L. Li, P.A. Salvador, G.S. Rohrer, *Nanoscale* **6**, 24 (2014)